



**HAL**  
open science

## **Water-in-PDMS emulsion templating of highly interconnected porous architectures for 3D cell culture**

Roberto Riesco, Louisa Boyer, Sarah Blossse, Pauline Lefebvre, Pauline Assemat,  
Thierry Leichle, Angelo Accardo, Laurent Malaquin

### ► **To cite this version:**

Roberto Riesco, Louisa Boyer, Sarah Blossse, Pauline Lefebvre, Pauline Assemat, et al.. Water-in-PDMS emulsion templating of highly interconnected porous architectures for 3D cell culture. *ACS Applied Materials & Interfaces*, 2019, 11 (32), pp.28631-28640. <10.1021/acsami.9b07564>. <hal-02379789>

**HAL Id: hal-02379789**

**<https://hal.science/hal-02379789v1>**

Submitted on 29 Nov 2019

**HAL** is a multi-disciplinary open access archive for the deposit and dissemination of scientific research documents, whether they are published or not. The documents may come from teaching and research institutions in France or abroad, or from public or private research centers.

L'archive ouverte pluridisciplinaire **HAL**, est destinée au dépôt et à la diffusion de documents scientifiques de niveau recherche, publiés ou non, émanant des établissements d'enseignement et de recherche français ou étrangers, des laboratoires publics ou privés.



HAL Authorization



## Open Archive Toulouse Archive Ouverte

OATAO is an open access repository that collects the work of Toulouse researchers and makes it freely available over the web where possible

This is an author's version published in: <https://oatao.univ-toulouse.fr/25123>

### Official URL:

<https://doi.org/10.1021/acsami.9b07564>

### To cite this version:

Riesco, Roberto and Boyer, Louisa and Blossse, Sarah and Lefebvre, Pauline M. and Assemat, Pauline and Leichle, Thierry and Accardo, Angelo and Malaquin, Laurent *Water-in-PDMS emulsion templating of highly interconnected porous architectures for 3D cell culture*. (2019) ACS Applied Materials and Interfaces, 11 (32). 28631-28640. ISSN 1944-8244

Any correspondence concerning this service should be sent to the repository administrator: [tech-oatao@listes-diff.inp-toulouse.fr](mailto:tech-oatao@listes-diff.inp-toulouse.fr)

# Water-in-PDMS Emulsion Templating of Highly Interconnected Porous Architectures for 3D Cell Culture

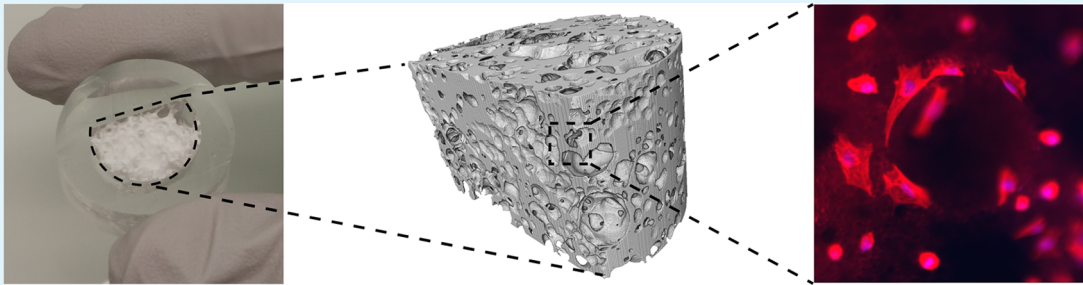
Roberto Riesco,<sup>†,‡</sup> Louisa Boyer,<sup>†</sup> Sarah Blossse,<sup>†,‡</sup> Pauline M. Lefebvre,<sup>§,||</sup> Pauline Assemat,<sup>§</sup> Thierry Leichle,<sup>†</sup> Angelo Accardo,<sup>\*,†,⊥</sup> and Laurent Malaquin<sup>\*,†</sup>

<sup>†</sup>LAAS-CNRS, Université de Toulouse, CNRS, F-31400 Toulouse, France

<sup>‡</sup>Institut National des Sciences Appliquées—INSA, F-31400 Toulouse, France

<sup>§</sup>Institut de Mécanique des Fluides de Toulouse, Université de Toulouse, CNRS, F-31400 Toulouse, France

<sup>||</sup>FR FERMAT, Université de Toulouse, CNRS, INPT, UPS, F-31400 Toulouse, France



**ABSTRACT:** The development of advanced techniques of fabrication of three-dimensional (3D) microenvironments for the study of cell growth and proliferation has become one of the major motivations of material scientists and bioengineers in the past decade. Here, we present a novel residueless 3D structuration technique of poly(dimethylsiloxane) (PDMS) by water-in-PDMS emulsion casting and subsequent curing process in temperature-/pressure-controlled environment. Scanning electron microscopy and X-ray microcomputed tomography allowed us to investigate the impact of those parameters on the microarchitecture of the porous structure. We demonstrated that the optimized emulsion casting process gives rise to large-scale and highly interconnected network with pore size ranging from 500  $\mu\text{m}$  to 1.5 mm that turned out to be nicely adapted to 3D cell culture. Experimental cell culture validations were performed using SaOS-2 (osteosarcoma) cell lines. Epifluorescence and deep penetration imaging techniques as two-photon confocal microscopy unveiled information about cell morphology and confirmed a homogeneous cell proliferation and spatial distribution in the 3D porous structure within an available volume larger than 1  $\text{cm}^3$ . These results open alternative scenarios for the fabrication and integration of porous scaffolds for the development of 3D cell culture platforms.

**KEYWORDS:** PDMS, 3D scaffold, emulsion, porosity, osteosarcoma cells

## 1. INTRODUCTION

23 The development of porous materials has been a major  
24 concern for materials science since decades. Their properties  
25 play an important role in many applications such as energy  
26 storage and conversion, pollutant gas capture, and drug  
27 delivery.<sup>1–4</sup> Porous structures are also fundamental in the  
28 development of living organisms. Oxygen capture in our bodies  
29 is due to the porosity of alveolar tissue in our lungs, which  
30 maximizes the exchange surface available for this task.<sup>5</sup> In  
31 bones, the trabecular topology works as a niche for the bone  
32 marrow and provides a proper environment for cellular  
33 regeneration.<sup>6</sup> Further, in the context of the realization of  
34 biomimetic scaffolds for cell culture and tissue engineering  
35 studies, the accurate tuning of pore distribution and pore size  
36 allows the cells to infiltrate easily within the material, promote  
37 the perfusion of nourishment, and facilitate the vascularization  
38 of the restored tissue.<sup>7</sup> To achieve these topologies, many

solutions have been recently proposed in the field of material  
sciences and, in particular, polymer science. 39 40

One of the most extended and widely used materials for  
bioapplications in the last decades is poly(dimethylsiloxane)  
(PDMS).<sup>8</sup> Since Wacker Chemie discovered this silicone-  
based organic elastomer in the 1950 s, it has found a large  
range of applications starting from lab on chips and  
microfluidic devices<sup>9</sup> to contact lenses, medical devices,<sup>10,11</sup>  
alimentary industry, passing through energy storage,<sup>12</sup> flexible  
electronics,<sup>13–15</sup> and piezoelectric actuators.<sup>16</sup> PDMS is also  
known for its biocompatibility<sup>17</sup> and molding properties<sup>18</sup> to  
generate medical devices or even bioimplants.<sup>19</sup> Furthermore, 50  
PDMS features a low surface tension and energy, and it is 51

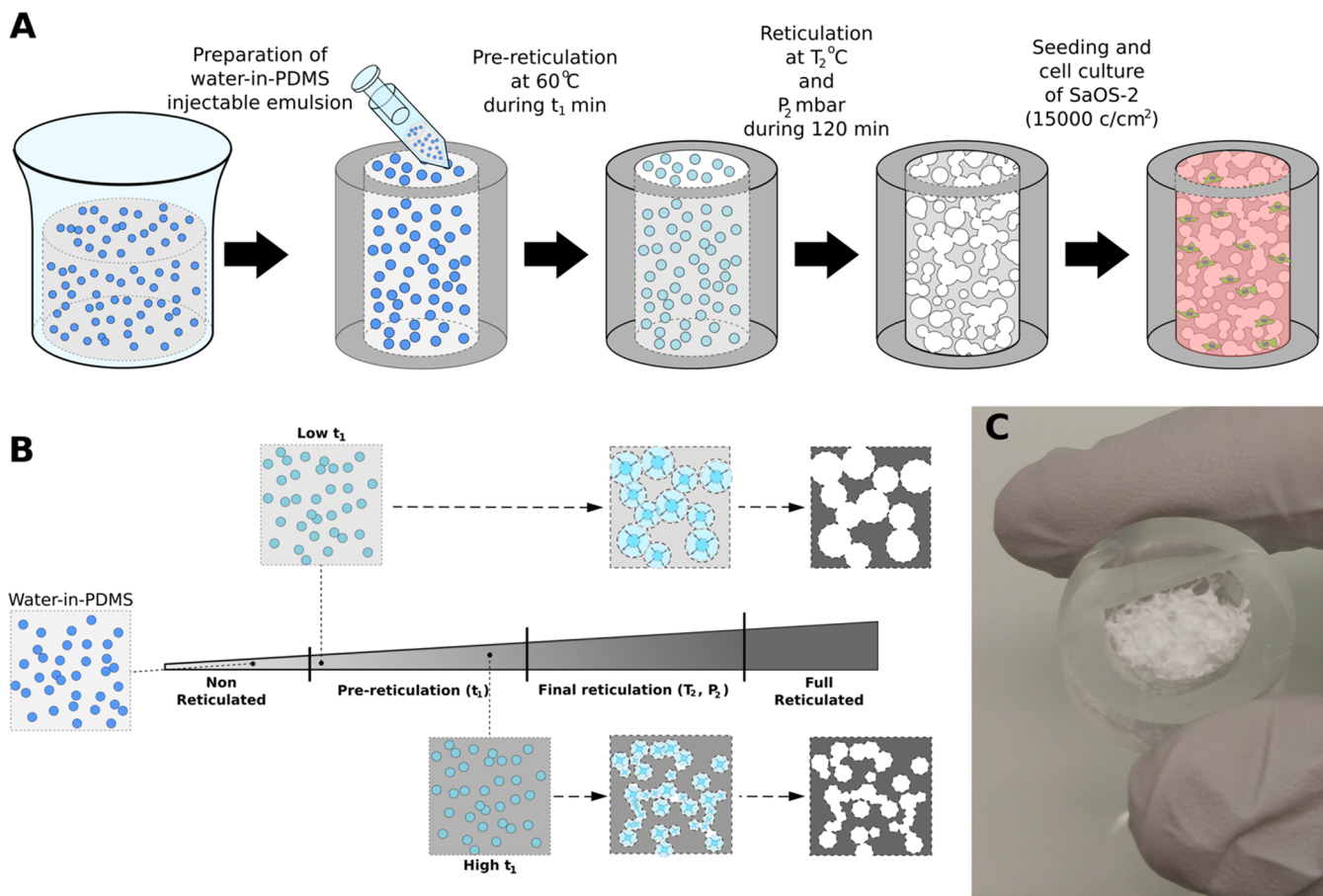


**Figure 1.** (A) Sketch of the fabrication process of the PDMS porous scaffold. The emulsion is injected into a PDMS shell and placed in an oven at 60 °C for  $t_1$  min. Afterward, the scaffolds are transferred to a vacuum oven at temperature  $T_2$  under pressure  $P_2$ . (B) Sketch of the impact of the physical parameters of the fabrication process in the porous morphology. (C) Optical image of the PDMS porous scaffold.

52 hydrophobic although its surface properties are easily tunable  
 53 via oxygen plasma treatment to introduce hydroxyl groups,  
 54 allowing grafting of proteins or other functional groups.<sup>20</sup>  
 55 Concerning biological applications, PDMS is well adapted  
 56 with cell biology applications:<sup>21</sup> it is compatible with almost  
 57 every technique of protein coating for cell adhesion, and its  
 58 mechanical properties<sup>18,22</sup> are known to be compatible with  
 59 cell culture. One of the main advantages over other materials is  
 60 its permeability to oxygen and water, which allows the cell  
 61 medium to oxygenate and reach biocompatibility levels.<sup>23</sup> In  
 62 addition, it is transparent and compatible with optical  
 63 characterization method and is lowly photoluminescent,<sup>24</sup>  
 64 allowing the use of fluorescent markers for the visualization of  
 65 cellular features. For all of these reasons, PDMS is broadly  
 66 used in biological applications and is undoubtedly one of the  
 67 main materials used in the fabrication of health sensors, flexible  
 68 biocontacts, or microfluidic devices for biomedical applica-  
 69 tions.

70 Nowadays, one of the main challenges in tissue engineering  
 71 is to develop models of microenvironments that mimic the key  
 72 aspects of the architecture and organization of living tissues.  
 73 Hence, in the past two decades, we witnessed a transition from  
 74 conventional two-dimensional (2D) Petri dish monolayer cell  
 75 culture approaches to three-dimensional (3D) architectures  
 76 featuring topological, mechanical, and biochemical aspects  
 77 matching the natural growth environment of cells.<sup>25–28</sup> To  
 78 fulfill this need, material scientists, biomedical engineers, and  
 79 microfabrication researchers started to investigate and develop

protocols aiming at realizing such architectures by exploiting  
 diverse additive manufacturing and other 3D fabrication  
 techniques such as fused deposition modeling and electro-  
 spinning,<sup>29</sup> stereolithography,<sup>30,31</sup> direct laser writing,<sup>32–35</sup>  
 or bioprinting.<sup>36</sup> Although most of these approaches allow the  
 fabrication of scaffold features down to the micrometric or  
 even submicrometric scale, they are often limited by the overall  
 printable size of the object, by the cost of the fabrication setup,  
 as well as by the scarcity of biocompatible materials for  
 biological applications.<sup>37</sup> PDMS can be hardly integrated  
 within additive manufacturing processes, and it is not possible  
 to unmold three-dimensional patterns with cell resolution  
 while its biocompatibility for biomedical applications is widely  
 proved. On the other hand, a large community of chemists and  
 material scientists developed fabrication protocols of PDMS  
 sponges based on emulsions/foams,<sup>38</sup> gas foaming,<sup>39</sup> or  
 microcasting of sacrificial materials/structures.<sup>40–43</sup> The  
 important molecular role of the hydrophobic/hydrophilic  
 tails and the tuning of its wettability properties<sup>44</sup> make it a  
 perfect candidate for microfluidic or environmental applica-  
 tions,<sup>45</sup> while some groups have recently tested the possibility  
 of using PDMS macroporous sponges for tissue engineer-  
 ing.<sup>46,47</sup>

In this paper, we report for the first time a simple, rapid, and  
 cost-effective 3D fabrication technique for creating mesoscale  
 porous PDMS scaffolds of centimeter scale, featuring a pore  
 size ranging from millimeter to micrometer scale. The protocol  
 is based on H<sub>2</sub>O/PDMS emulsion casting and subsequent

108 pressure-/temperature-controlled curing. This process is  
109 similar to previously reported polymer high internal phase  
110 emulsion (polyHIPE) technique;<sup>48,49</sup> however, it relies on a  
111 progressive expansion of the internal phase that allowed us to  
112 tune the pore size, distribution, and interconnectivity within  
113 the architecture. Optical microscopy, scanning electron  
114 microscopy (SEM), and X-ray tomography investigations  
115 showed an interconnected porous architecture with an  
116 available porosity estimated to be higher than 57%. The  
117 scaffolds were then tested in the presence of an osteosarcoma  
118 cell line, namely, SaOS-2, which holds several osteoblastic  
119 features<sup>50</sup> and is commonly employed as an in vitro model for  
120 studying the transition of human osteoblasts to osteocytes.<sup>51</sup>  
121 The SEM, fluorescence, and two-photon confocal imaging  
122 characterizations of both the surface and the inner core of the  
123 scaffold revealed an efficient 3D cell colonization of the  
124 architecture and the presence of the typical flattened  
125 cytoskeletal morphology expected for SaOS-2 cells. The results  
126 show how the fast prototyping fabrication protocol that we  
127 developed and the tunability of the pore size and pore  
128 distribution open a promising scenario for the development of  
129 3D cell culture models and tissue engineering applications  
130 involving PDMS.

## 2. MATERIALS AND METHODS

131 **2.1. Materials.** Poly(dimethylsiloxane) (PDMS) was purchased  
132 from Dow Corning in a kit containing a silicone base and a curing  
133 agent (Sylgard 184). All of the PDMS mixtures presented in this work  
134 were prepared following standard proportions (10:1 = base/curing  
135 agent w/w) and properly degassed using a dedicated chamber under  
136 vacuum. We employed ultrapure (type I) deionized water (DIW)  
137 from a Milli-Q Direct purifier system. Molds were fabricated with a  
138 3D stereolithographic system DWS 29J+ in DS3000 and DL260  
139 materials from DWS Systems.

140 **2.2. Fabrication of Standardized PDMS Scaffold Holders.**  
141 Due to the biological purposes of this work, the dimensions of all of  
142 the developed scaffolds were designed to be compatible with standard  
143 cell culture consumables configuration. The samples were fabricated  
144 to fit inside a 12-well plate (22 mm diameter for each well). To ensure  
145 a perfect sealing of the scaffold in the wells and provide a manageable  
146 object, a PDMS scaffold holder was fabricated by 3D printing and  
147 inserted in the multiwell plate during the casting (see Figure S1 in the  
148 Supporting Information) to obtain a cylindrical shell of PDMS with a  
149 semicircular empty space where we then injected the water/PDMS  
150 emulsion. The height of the scaffold holder was set between 1 and 1.5  
151 cm, while its inner diameter was set to 1.4 cm. PDMS silicone was  
152 poured on the plate and cured at 60 °C overnight.

153 **2.3. Emulsion Casting.** Highly porous PDMS scaffolds were  
154 fabricated by the method of emulsion casting, using water as internal  
155 phase, and reticulating the emulsion within specific environmental  
156 conditions (Figure 1A,B). Water-in-PDMS emulsion was made by  
157 progressively adding small quantities (~10% of PDMS mass) of DIW  
158 and mixing until reaching 70% of water-in-silicone. With this process,  
159 we generated a water-in-silicone emulsion that was then injected into  
160 the cylindrical sample holder. The reticulation process consisted of  
161 two separate steps of reticulation by varying temperatures and  
162 pressures that allowed us to control the pore size and distribution  
163 (Figure 1C): (1) the samples were first placed inside an oven  
164 (Memmert) at  $T_1 = 60$  °C for a specific time  $t_1$  ranging from 30 to 60  
165 min in atmospheric pressure condition; (2) the samples were then  
166 transferred into a vacuum oven (SalvisLAB Vacucenter) at  $T_2$  ranging  
167 between 110 and 130 °C with an absolute pressure value  $P_2$  of 400 or  
168 700 mbar for 2 h. After this time, we did not observe any notable  
169 evolution of the size and interconnectivity of the pores. Both edges of  
170 the samples were removed by slicing the cylinder with a surgical blade  
171 to obtain a clean surface.

**2.4. Scanning Electron Microscopy.** We used scanning electron  
172 microscopy (SEM) to observe the microscopic morphology of the  
173 samples with a Hitachi S-4800 system at an accelerating voltage  
174 ranging from 2 to 5 kV and 10  $\mu$ A current. The imaging was  
175 performed on core regions of the scaffolds, accessed by cross-cutting  
176 the samples with a surgical blade, in flat and 45° tilt-angle SEM  
177 sample holder positioning configuration. To improve the resolution  
178 and avoid charging effects, the samples were coated with a 15 nm  
179 layer of sputtered gold using PECS I from Gatan Systems. False-color  
180 imaging treatment was performed by using the open-access software  
181 Gimp 2. 182

**2.5. X-ray Tomography.** To investigate the pore properties of the  
183 sample, X-ray microcomputed tomography ( $\mu$ CT) imaging was  
184 performed.  $\mu$ CT is a nondestructive imaging technique that allows  
185 quantification of internal features of an object in three dimensions  
186 with microscopic resolution. In this study, the specimen was inserted  
187 inside a X-ray microtomography machine manufactured by RX  
188 Solutions (EasyTom XL 150). A sealed-type microfocus X-ray source  
189 with beryllium target was used. The X-ray source energy was adjusted  
190 to the resolution of the scan: the source voltage was fixed at 66 kV  
191 and source current at 268  $\mu$ A. Before the acquisition, standard black  
192 and gain calibrations were performed. A complete scan was acquired  
193 by recording 1440 projections of the sample at different angles,  
194 equally spaced on 360°, with a flat panel of 1920  $\times$  1536 pixels. Each  
195 projection had average exposure times of 0.11 and 5 s. The 3D  
196 volume and corresponding slices were reconstructed with the RX  
197 Solutions software, X-Act, using a filtered back-projection algorithm.  
198 Reconstructed slices had an isotropic resolution of 18  $\mu$ m. 199  
200 Postprocessing of images was performed with Avizo 9.7.0, a software  
201 dedicated to data visualization, segmentation, and quantification. A  
202 nonlocal means filter<sup>52</sup> was first used to remove noise. For the  
203 binarization of images, two different methods were used: (1) a user-  
204 defined threshold was applied to separate pores and PDMS matrix  
205 and extract the binary image on each slice; (2) a watershed  
206 algorithm<sup>53</sup> was also applied on filtered images to separate pores  
207 and PDMS material. Watershed-based segmentation consists of  
208 transforming the gray-level image as a topographic map, where high  
209 intensity represents peaks and hills while low intensity represents  
210 valleys. The obtained topographic image is then flooded, starting from  
211 user-defined seeds, using an automatic gradient magnitude algorithm.  
212 Dams are built to avoid merging water from two different catchment  
213 basins. The segmentation result is defined by the locations of the  
214 dams, i.e., the watershed lines. Porosity in both cases (user-defined  
215 threshold and watershed algorithm) was finally calculated as the  
216 fraction of pore volume over the total volume of the specimen. The  
217 connectivity of pores was evaluated with the Axis Connectivity  
218 function available on Avizo.

**2.6. Water Retention.** To complement the results obtained by X-  
219 ray microcomputed tomography, an empirical test was completed to  
220 provide experimental data about the absorbance of water within the  
221 3D architecture. The porous PDMS scaffolds were dried in a vacuum  
222 oven at 60 °C overnight and then weighted to obtain  $W_{dry}$ . The  
223 PDMS was plasma-activated using oxygen plasma treatment (Diener  
224 Electronic, 5 sccm oxygen flow, 0.5 mbar, 5 min, 50 W) to enhance  
225 wettability and immediately soaked in PBS over 48 h. The water  
226 retained in the scaffold was measured using an electronic balance that  
227 provided us with  $W_{wet}$ . The percent of water remaining in the porous  
228 PDMS scaffold was calculated as<sup>54</sup> 229

$$\text{water retention (\%)} = \frac{(W_{wet} - W_{dry})}{W_{dry}} \times 100$$

**2.7. Cell Culture, Fixation, and Staining.** Prior to cell culture, 230  
231 the porous PDMS scaffolds were first sterilized for 1 h under UV  
232 exposure at 254 nm. The PDMS surface was then activated with an  
233 oxygen plasma treatment (Diener Electronic, 5 sccm oxygen flow, 0.5  
234 mbar, 5 min, 50 W) and coated with 10  $\mu$ g/mL of human fibronectin  
235 (Corning) for 1 h at room temperature. The osteosarcoma cell line  
236 (SaOS-2) was obtained from the American Type Culture Collection  
237 (ATCC) and grown using minimum essential medium  $\alpha$  ( $\alpha$ -MEM) 237

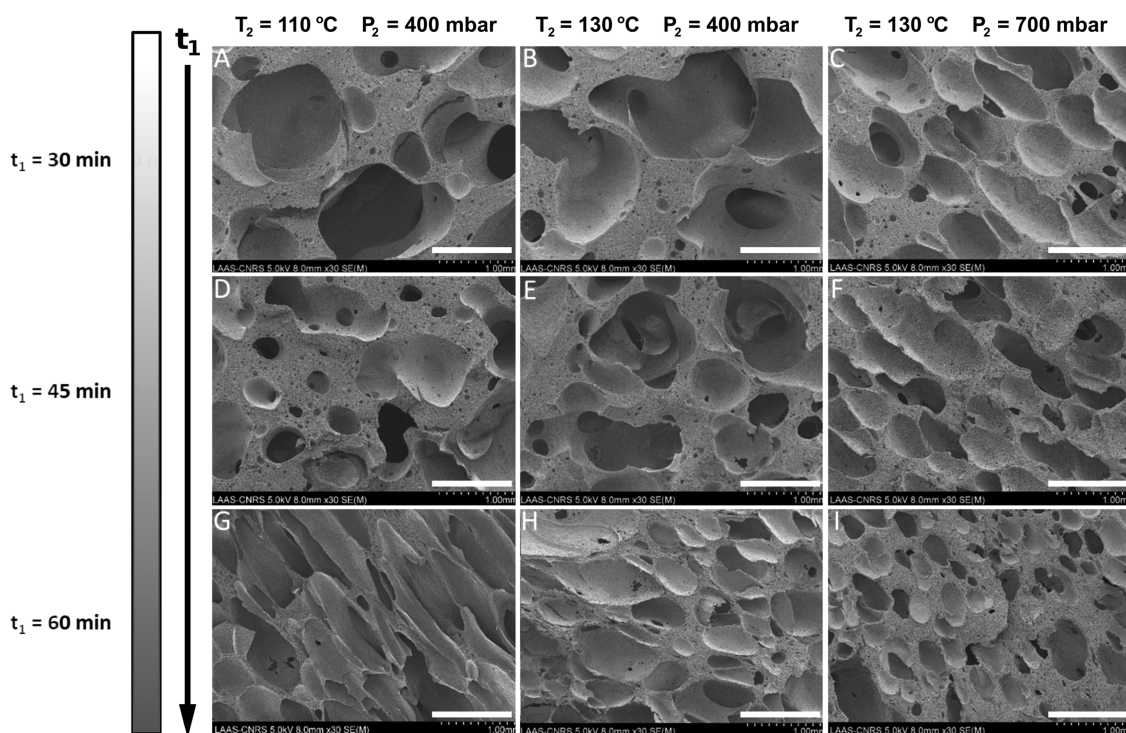


**Figure 2.** SEM characterization of the cross-sectional regions in the PDMS porous scaffold for different curing parameters. Along the vertical axis, we vary the time  $t_1$  for the prereticulation stage at 60 °C. Along the horizontal axis, we vary the temperature  $T_2$  and the pressure  $P_2$  of the second reticulation process. The scale bar is 1 mm.

238 containing nucleosides, GlutaMAX, (Gibco, Fisher Scientific)  
 239 supplemented with 10% fetal bovine serum (HyClone, Fisher  
 240 Scientific) and 1% penicillin/streptomycin mix (Gibco, Fisher  
 241 Scientific). A cell suspension (15 000 cells/cm<sup>2</sup>) was deposited in a  
 242 droplet of supplemented  $\alpha$ -MEM on top of the PDMS porous scaffold  
 243 and incubated in an atmosphere containing 5% CO<sub>2</sub> at 37 °C for 1 h  
 244 to enable the cells to adhere to the scaffold. Multiwell plates were then  
 245 filled with additional supplemented  $\alpha$ -MEM and incubated for 72 h.  
 246 To prepare the sample for SEM characterization, cells were rinsed  
 247 with PBS 1 $\times$  (phosphate-buffered saline) solution and incubated in  
 248 4% glutaraldehyde (Sigma) solution for 4 h at room temperature. The  
 249 cells were then dehydrated by incubation in 50, 70, 90, and 100%  
 250 ethanol solutions for 4 min at each step and dried for few hours at  
 251 room temperature to remove alcohol residues. Immunofluorescence  
 252 staining was performed as follows: cells were rinsed with PBS 1 $\times$ ,  
 253 fixed with 10% formalin solution (Sigma) for 30 min, permeabilized in  
 254 0.2% Triton X-100 for 3 min, and blocked in 3% BSA for 30 min. The  
 255 samples were then incubated in phalloidine-rhodamine (Invitrogen,  
 256 Fisher Scientific) at 1/200 dilution in PBS 1 $\times$  for 30 min at 37 °C to  
 257 stain the F-actin (protein of the cell cytoskeleton) and then in a DAPI  
 258 (Thermo Scientific, Fisher Scientific) solution at 1/100 dilution in  
 259 PBS 1 $\times$  for 5 min at room temperature to stain the DNA in the  
 260 nuclei. After staining, the cells were stored in PBS 1 $\times$  solution at 4 °C.  
 261 In an additional protocol for two-photon confocal imaging, the cells  
 262 were rinsed with PBS 1 $\times$ , stained with a mix of Hoechst (Invitrogen,  
 263 Fisher Scientific) at 5  $\mu$ g/mL plus CMFDA (Invitrogen, Fisher  
 264 Scientific) at 1/1000 dilution in DMEM without phenol red (Gibco,  
 265 Fisher Scientific), incubated for 30 min at 37 °C, rinsed again with  
 266 PBS 1 $\times$ , and fixed for 30 min in 10% formalin solution (Sigma). The  
 267 samples were stored in PBS 1 $\times$  at 4 °C prior to imaging.  
 268 Cytocompatibility was assessed by Live/Dead assay in the porous  
 269 PDMS scaffold choosing flat PDMS and glass as control. All samples  
 270 followed the protocol of plasma treatment and fibronectin coating  
 271 mentioned above. After 72 h of culture in supplemented  $\alpha$ -MEM, the  
 272 samples were rinsed in PBS and cells were stained with calcein/  
 273 ethidium (Live/Dead viability kit for mammalian cells, Fisher

Scientific) diluted in DMEM without phenol red for 30 min and 274  
 then rinsed with the same medium for fluorescence characterization. 275

**2.8. Immunofluorescence Characterization.** Two different 276  
 immunofluorescence imaging techniques were employed to investi- 277  
 gate the cell distribution and proliferation taking place on the 3D 278  
 PDMS scaffolds. 2D observations of the scaffolds' surface were 279  
 performed using an Olympus C211 fluorescence microscope 280  
 equipped with a X-Cite 120 Hg lamp, a BP (300–400 nm) filter 281  
 for DAPI, a BP (575–595 nm) filter for calcein, a BP (518–573 nm) 282  
 filter for phalloidin rhodamine/ethidium, and 5 $\times$ , 10 $\times$ , 20 $\times$  and 50 $\times$  283  
 objectives. 3D imaging of the scaffolds were performed using a two- 284  
 photon confocal imaging system (AxioImager upright microscope 285  
 LSM 7MP, Carl Zeiss). A pulsed femtosecond Ti:sapphire laser 286  
 (Chameleon Ultra II; Coherent) tunable in the range of 690–1064 287  
 nm was used as excitation light source. Z-stack acquisitions were 288  
 performed with a 10 $\times$  W-Plan Apochromat air objective with 0.45 289  
 N.A. and a laser excitation wavelength tuned at 800 nm. An automatic 290  
 z-compensation of the laser power was applied to provide a 291  
 homogeneous imaging of the imaged volume of the 3D scaffold. 292  
 Emitted light was detected through a descanned pathway leading to 293  
 two nondescanned detectors and emission was recorded simulta- 294  
 neously with two emission filters: a band pass (BP) filter, set at 500– 295  
 550 nm (green channel, CMFDA), and a short-pass (SP) filter set at 296  
 485 nm (blue channel, DAPI). Image processing and 3D 297  
 reconstruction were performed by ImageJ and Imaris (Version 8.2, 298  
 Bitplane) softwares. 299

### 3. RESULTS AND DISCUSSION

**3.1. Morphological Characterization of the PDMS** 300  
**Scaffolds.** In Figure 2, we report how the tuning of the 301  
 fundamental curing parameters ( $t_1$ , along the vertical axis, and 302  
 $T_2$ – $P_2$ , along the horizontal axis) affects the morphology of the 303  
 PDMS porous scaffolds. The increment of the prereticulation 304  
 process time affects the pore size and distribution as 305  
 highlighted by comparing the rows of each column. The first 306  
 row of Figure 2A–C, related to  $t_1 = 30$  min, shows a typical 307

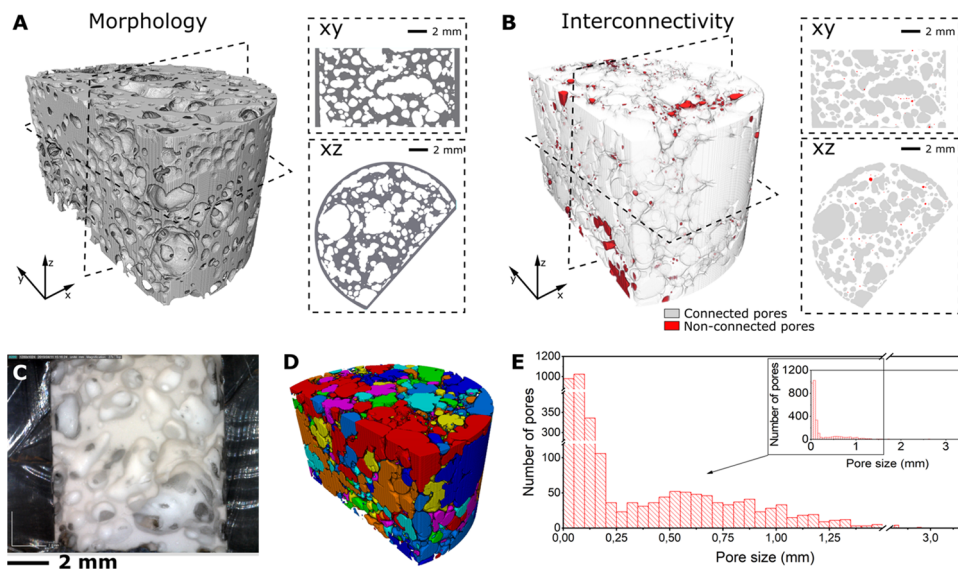


**Figure 3.** (A) 3D view of the PDMS scaffold after segmentation process. On the right, crosscuts of the reconstruction along the  $xy$  and  $xz$  planes. (B) 3D view of the pores: nonconnected pores (red), connected pores (white). On the right, crosscuts of the reconstruction along the  $xy$  and  $xz$  planes. (C) Optical micrograph of the inner core of a PDMS porous scaffold. (D) 3D colorimetric view of the pores size distribution with a watershed-based algorithm. (E) Distribution of the number of pores according to the pore size depicted in (D).

308 pore size of 1–3 mm with few submillimetric pores observable.  
 309 When increasing  $t_1$  up to 45 min, this pore size distribution  
 310 slightly decreases (Figure 2D–F) down to 0.5–2 mm, while  
 311 we observe at the same time an increased number of  
 312 submillimetric pores. Finally, in the third row of Figure 2G–  
 313 I, we report a reduction of the pore size coupled to an evident  
 314 anisotropy of the pore orientation directed toward the open  
 315 side of the PDMS scaffold holder.

316 A lower  $t_1$  implies a less reticulated state of the PDMS within  
 317 the emulsion when starting the final curing process. We then  
 318 attribute the presence of large pore size (Figure 1A–C) to the  
 319 easier expansion of the water steam in a less reticulated PDMS.  
 320 We believe that this factor may induce the aggregation of  
 321 submillimetric water bubbles and the consequent formation of  
 322 larger cavities.

323 By comparing the first column (A, D, G) and second column  
 324 (B, E, H) of Figure 2, we investigate the impact of the different  
 325 temperatures  $T_2$  (110 and 130 °C) employed in the second  
 326 reticulation process. By fixing  $t_1 = 30$  min, we cannot find  
 327 striking differences in pore size in Figure 2A,B, while this  
 328 difference becomes more evident for higher prereticulation  
 329 periods, as reported in Figure 2D–F. In Figure 2G, we can  
 330 observe strong anisotropy, with elongated pores whose main  
 331 semiaxis is 2- to 3-fold larger than the minor semiaxis. The  
 332 pores of Figure 2F show lower anisotropy compared to Figure  
 333 2G but still much higher than the one of the pores in Figure  
 334 2B,E. We suggest that the temperature of final reticulation ( $T_2$ )  
 335 has a double impact on the reaction: on the one hand, it  
 336 slightly modifies the speed of evaporation of the water bubbles;  
 337 on the other hand, it varies the kinetics of the reticulation of  
 338 the silicone. As we observe from the comparison of Figure  
 339 2G,H, a lower temperature indeed tends to benefit the  
 340 appearance of intrinsic anisotropy of the sample, which can be  
 341 linked to a higher state of reticulation during the expansion of  
 342 the water steam bubbles.

343 The third column (Figure 2C,F,I) explores the same  
 344 temperature  $T_2$  (130 °C) as in the second column (Figure  
 345 2B,E,H) but with a different pressure  $P_2$  (700 mbar instead of

400 mbar). By observing the samples obtained with a short  
 346 prereticulation time  $t_1$  (Figure 2B,C), it is possible to highlight  
 347 the impact of the pressure over the pore size. While the sample  
 348 2B features an average pore size of 1–3 mm, sample 2C  
 349 presents a critical decrease of the typical size to 0.7–1.2 mm.  
 350 For  $t_1 = 45$  min, we observe the same tendency of reduced  
 351 typical pore size within the PDMS porous scaffold, although  
 352 this transition is less evident for the samples at 700 mbar  
 353 (Figure 2C,F) than for the samples at 400 mbar (Figure 2B,E).  
 354 Concerning the last row (Figure 2H,I), at long prereticulation  
 355 time (60 min), we perceive a major reduction on the pore size  
 356 coupled to a slight decrease in anisotropy of the pores. This  
 357 behavior fits with the results obtained in the rest of the samples  
 358 for those parameters.  
 359

The general overview of Figure 2 shows then a progressive  
 360 decrement of the pore size by increasing the time of  
 361 prereticulation  $t_1$ , which leads, at the same time, to an increase  
 362 of the number of pores. We observe also an anisotropy  
 363 tendency linked to the reticulation time (i.e., longer  $t_1$   
 364 increases the reticulation state of the silicone before the  
 365 evaporation of the steam). This induces less motility in the  
 366 emulsion that in turn leads to a further expansion of the  
 367 bubbles in the direction of the apertures of the PDMS sample  
 368 holder. Temperature  $T_2$ , on the other hand, plays a dual role in  
 369 the kinetics of the water evaporation and the kinetics of the  
 370 reticulation process within the emulsion. Finally, pressure  $P_2$   
 371 hinders the expansion of the bubbles, limiting the final pore  
 372 size. From a microscopic point of view, the PDMS porous  
 373 scaffold presents a hierarchical porous structuration. A close-up  
 374 view of the bulk material between the larger pores for different  
 375 fabrication parameters ( $t_1$ ,  $T_2$ ,  $P_2$ ) reveals a network of  
 376 interconnected pores featuring smaller dimensions (5–30  $\mu\text{m}$ )  
 377 with openings of 1–5  $\mu\text{m}$  (see Figure S2). This induces a  
 378 roughness on the surface that might influence the perfusion  
 379 and diffusion of culture medium with a global impact for the  
 380 cell environment.  
 381

To provide a more quantitative analysis of the pore size and  
 382 spatial distribution, we performed a characterization of the  
 383

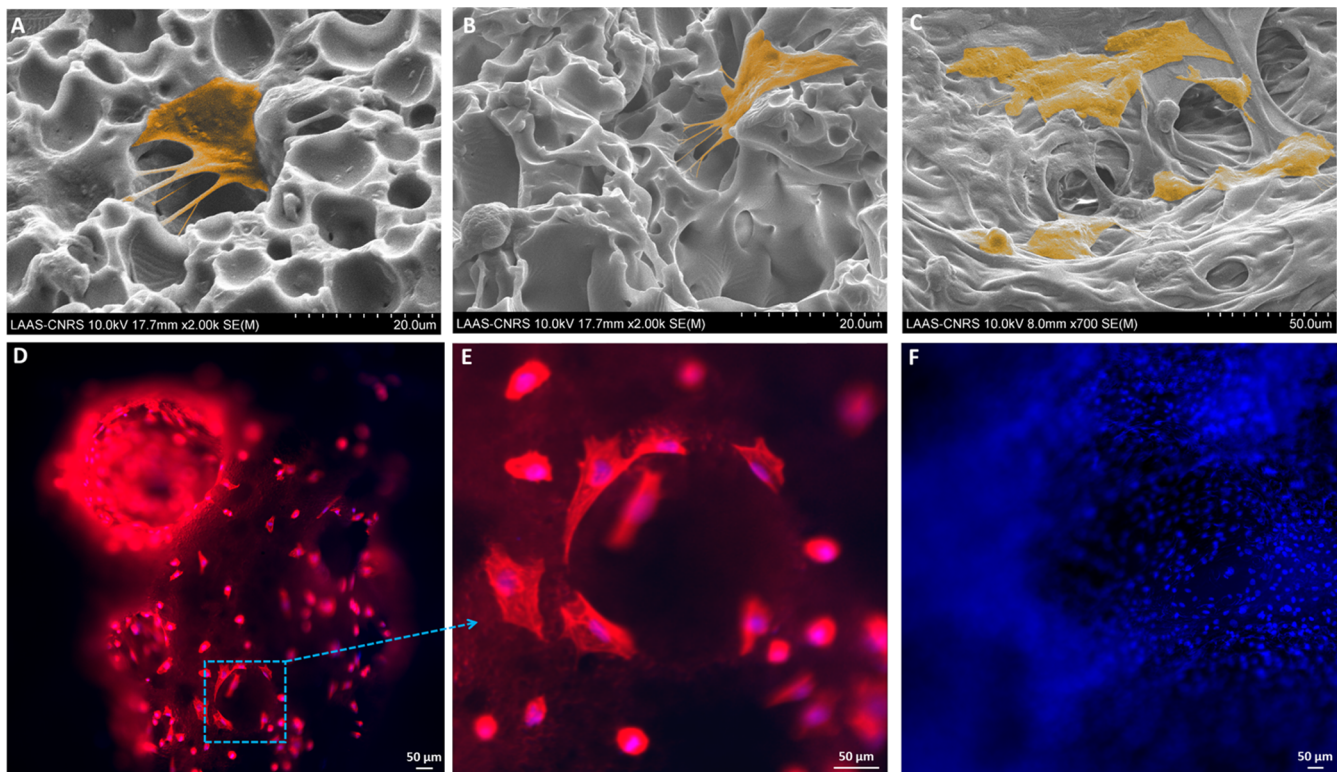


**Figure 4.** (A–C) False-colored SEM images highlighting the SaOS-2 cell morphology obtained on the PDMS porous scaffold; (D) immunofluorescence imaging of SaOS-2 cells colonizing the pores of the porous PDMS scaffold; (E) close-up view on the region enclosed in the blue dotted square in (D); (F) SaOS-2 “cellular-carpet” observed on the PDMS porous scaffold surface (red: phalloidin-F-actin; blue: DAPI-nuclei).

384 PDMS porous scaffold by employing X-ray tomography. The  
 385 selected sample corresponds to the one of Figure 2B with  $t_1 =$   
 386 30 min,  $T_2 = 130$ , and  $P_2 = 400$  mbar, which was then  
 387 employed as 3D cell culture support.

388 Figure S3A shows a reconstructed slice of the sample, after  
 389 denoising with a nonlocal means filter. A user-defined  
 390 threshold was applied on each slice of the sample, leading to  
 391 a stack of binarized images, as presented Figure S3B,  
 392 corresponding to the slice shown in Figure S3A. The 3D  
 393 reconstructed view of the PDMS porous scaffold in Figure 3A  
 394 shows the porosity of the 3D architecture (whose optical  
 395 micrograph is reported in Figure 3C). The crosscut views for  
 396 the  $xy$  and  $xz$  planes show the inner core of the 3D  
 397 architecture, proving a highly interconnected network with a  
 398 wide spectrum of porosity. From those data, a porosity equal to  
 399 around 57% was calculated from the binarized images (Figure  
 400 S3C). A second validation of porosity using a watershed  
 401 segmentation algorithm (for details, see Materials and  
 402 Methods) was performed, resulting in a porosity equal to  
 403 58.7%, as presented in Figure 3D. Connectivity of pores was  
 404 also studied with the Axis Connectivity module available in  
 405 Avizo. Figure 3B shows in red the nonconnected pores and in  
 406 white the connected ones. The total volume of pores is equal  
 407 to  $406.2 \text{ mm}^3$  in the sample, and nonconnected pores  
 408 represent only  $4.3 \text{ mm}^3$ , corresponding to 1% of the total  
 409 volume of pores. Nonconnected pores are either small pores  
 410  $<100 \mu\text{m}$  in the matrix or pores that are localized in the walls  
 411 of the cylindrical support.

412 Finally, pore size distribution was analyzed. The histogram  
 413 plot in Figure 3E represents the distribution of pore equivalent  
 414 diameter, whose colorimetric 3D visualization linking pore

diameters to different colors is reported in Figure 3D. The  
 415 majority of the pores were reported to have a diameter  
 416 between 0.02 and 0.10 mm (more detailed histograms are  
 417 reported in Figure S4), although smaller pores (observed by  
 418 SEM, Figure S2) could not be resolved due to resolution  
 419 limitation ( $18 \mu\text{m}$ ) of the X-ray microcomputed tomography  
 420 setup (see Materials and Methods). These results were  
 421 complemented with measurements of water retention  
 422 performed over 48 h in the porous PDMS scaffold. As  
 423 shown in Figure S5 and in the Supporting Video “Video\_  
 424 liquid\_loading”, the percent of water remaining in the scaffold  
 425 after soaking it in PBS for different periods of time increases  
 426 until reaching a value close to  $\sim 300\%$  (w:w). This value agrees  
 427 with the high porosity and interconnectivity estimated by  $\mu\text{CT}$ .  
 428

### 3.2. SEM and Immunofluorescence Characterization of SaOS-2 Cell Colonization of the PDMS Scaffolds.

To validate the compatibility of the developed PDMS architec-  
 431 tures as a 3D cell culture tool, we tested the scaffold topology  
 432 depicted in Figure 2B in the presence of SaOS-2 cells. Due to  
 433 the morphology of the SaOS-2 cells and the topographical  
 434 features of the PDMS porous scaffold, distinguishing the cells  
 435 directly over a rugose surface is a laborious task. This is evident  
 436 after comparing the morphologies of the osteosarcoma SaOS-2  
 437 cell line on untreated PDMS flat surfaces (Figure S6A) and on  
 438 plasma treated/fibronectin-coated PDMS surfaces (Figure  
 439 S6B). While on untreated surfaces we observe the same ratio  
 440 of cells holding the expected flattened morphology and the less  
 441 conventional globular one, on the treated surfaces we report  
 442 only the flattened cytoskeletal configuration coupled to a more  
 443 marked expression of typical round protrusions already  
 444 observed elsewhere.<sup>55</sup> In such context, the role of roughness 445

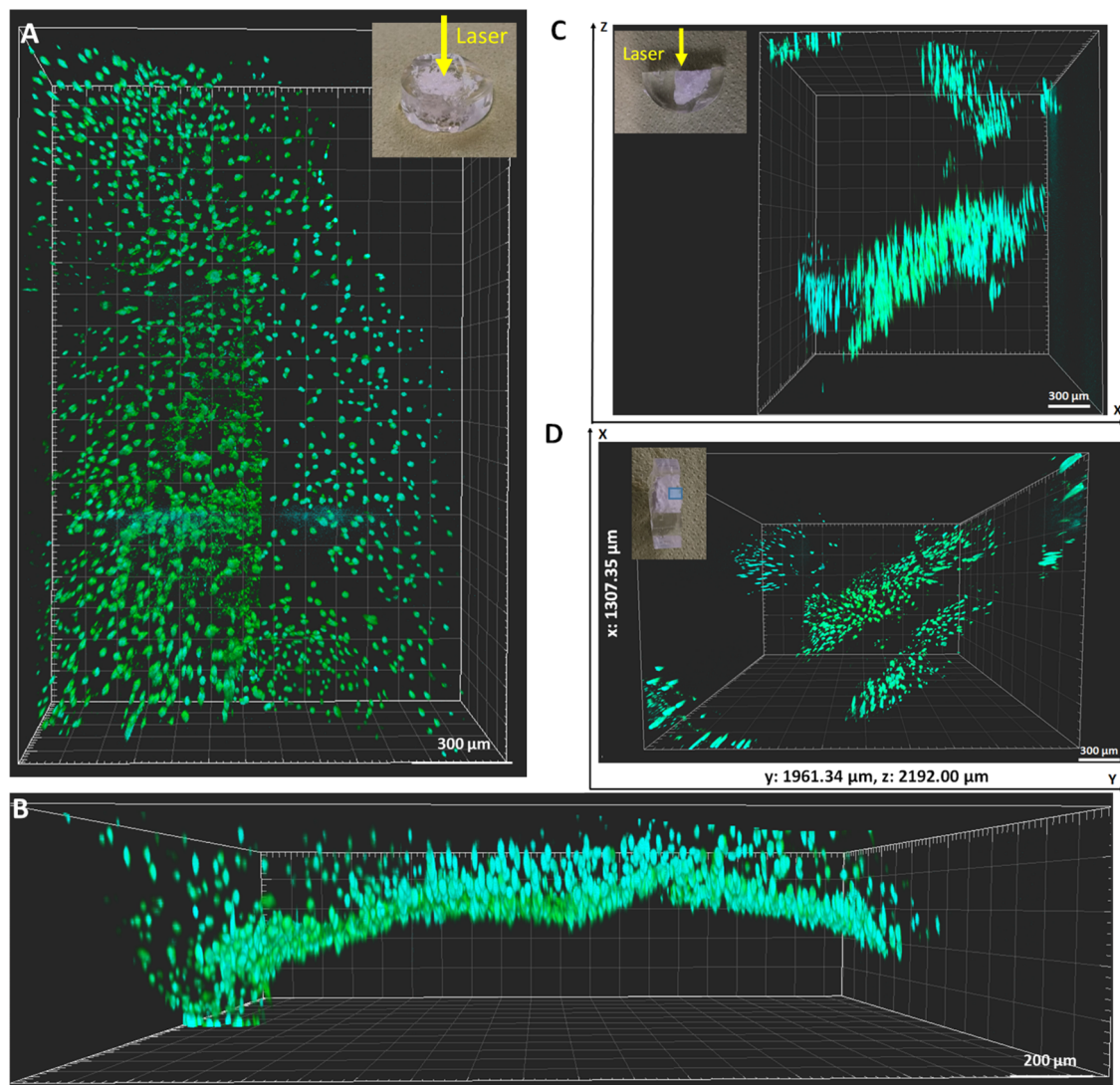


**Figure 5.** Two-photon confocal imaging of the PDMS porous scaffold colonized by SaOS-2 cells. (A) *xy* view of the 3D reconstruction of the scaffold imaged with the laser beam impinging the sample as shown in the inset; (B) *xz* view of the 3D reconstruction in (A); (C) *xz* view of the 3D reconstruction of a cross-cut of the scaffold imaged with the laser beam impinging the sample as shown in the inset; (D) *xy* view of the 3D reconstruction in (C) (the inset shows the sample orientation and the region depicted in the 3D reconstruction (green: CMFDA; blue: DAPI-nuclei)).

446 and surface chemistry regulating cell adhesion mechanisms has  
447 been previously observed for nonpolymeric surfaces.<sup>56,57</sup>

448 In addition to its role in the adsorption of adhesion proteins,  
449 plasma treatments are indeed known to induce the presence of  
450 nanotopography features and surface chemistry changes, which  
451 are reflected in an augmentation of oxygen content and an  
452 enhancement of surface energy associated with an increase in  
453 wettability that influences cell adhesion on polymeric  
454 surfaces.<sup>58,59</sup> Concerning the distribution and welfare of cells  
455 within the PDMS porous scaffold, in Figure 4A–C, we present  
456 false-colored SEM close-up images highlighting the typical cell  
457 morphology that we observed in different regions of the  
458 scaffold. SaOS-2 cells tend to develop cytoskeletal extensions  
459 anchoring to the side walls of the micropores in a  
460 tridimensional spatial configuration, as observed in Figure  
461 4A,B. The evidence of the flattened elongated morphology of a  
462 cluster of cells in other regions of the scaffold characterized by  
463 PDMS meshes is shown in Figure 4C. Furthermore, we can  
464 discriminate several round protuberances within the cellular

465 cytoskeleton that we associate with regular features of  
466 mineralized buds and calcospherulites related to the process  
467 of mineral deposition of this cell line.<sup>60,61</sup> This behavior could  
468 be associated with a predifferentiation stage, although a deeper  
469 evaluation of differentiation markers is required to confirm this  
470 assessment. Prospective analysis of the calcification process by  
471 red alizarin staining will be carried out in the future to validate  
472 this conclusion. Furthermore, cell viability test, shown in  
473 Figure S7, was addressed by Live/Dead assay on the porous  
474 PDMS scaffold against two positive controls, flat PDMS and  
475 glass. Cell viability reached ~99% of the cell population over  
476 the porous PDMS scaffold. This result compares with the  
477 performance of both positive controls showing as well a cell  
478 viability of ~99% and a more homogeneous cell distribution.

479 To better visualize typical morphological features of the  
480 SaOS cells cultured on the 3D scaffold, in Figure 4D–F, we  
481 report the epifluorescence characterization of the osteosarcoma  
482 cells over the PDMS porous scaffold. In Figure 4D, we can  
483 observe the cell spreading and colonization of different pores,

484 where the F-actin, the main component of microfilaments in  
485 the cytoskeleton, is stained in red with phalloidin/rhodamine  
486 while the nuclei are stained in blue with DAPI. We can  
487 distinguish several cells colonizing the full structure at different  
488 out-focus planes. In Figure 4E, we show the close-up view of a  
489 single pore (enclosed by the blue square in Figure 4D)  
490 depicting how the elongated cytoskeleton of the cells adapts to  
491 the surrounding environments by following the geometrical  
492 profile of the pore. Finally, in Figure 4F, we present a  
493 fluorescence image of another region of the scaffold where we  
494 can easily identify cell nuclei and observe how cells cover  
495 homogeneously the whole surface of the PDMS porous  
496 scaffold.

497 To get a clear view of the 3D cell colonization scenario of  
498 the PDMS porous scaffold, in Figure 5, we report several 3D  
499 reconstructions obtained via two-photon confocal imaging, a  
500 widely used technique for unveiling cell features in the inner  
501 core of 3D architectures otherwise not accessible by more  
502 conventional morphological imaging approaches (e.g., SEM  
503 and AFM).<sup>33,35</sup> In Figure 5A,B, we report the characterization  
504 of the upper part of the 3D scaffold (i.e., the one on which the  
505 cell medium containing the SaOS-2 cells was deposited),  
506 impinged by the laser beam as shown in the inset of Figure 5A,  
507 where we highlighted the nuclear marker DAPI (in blue) and  
508 the CMFDA one (in green), which is able to stain the whole  
509 cytoplasm of the cells (Figure S8). The overall field of view of  
510 the acquisition is  $1.96 \times 1.30 \times 0.49 \text{ mm}^3$  (obtained by  
511 employing a mosaic modality where we imaged smaller areas  
512 and then stitched them together). Figure 5A shows a quite  
513 homogeneous cell coverage of the PDMS scaffold surface,  
514 while Figure 5B highlights how cells are able to colonize the  
515 inner part of the architecture by infiltrating open pores (such  
516 as the one on the left-hand side of the figure). We attribute the  
517 absence of cells in the central part of the 3D reconstruction  
518 either to the small dimensions of the pores (compared to the  
519 SaOS-2 cell size) in that region or, more likely, to the fact that  
520 denser regions of PDMS (becoming opaque during the  
521 fabrication because of the trapping of air bubbles) hinder the  
522 passage of photons. A clearer overview of the 3D imaging  
523 acquisition can be seen in the Supporting Video “Video\_  
524 top\_surface”. To have a further insight into the cellular  
525 distribution within the 3D scaffold, we performed also a cross-  
526 cut on it by using a surgical blade to reveal the inner part of the  
527 structure. Figure 5C,D shows, respectively, the  $x$ ,  $z$  and  $x$ ,  $y$   
528 views of a  $1.30 \times 1.96 \times 2.19 \text{ mm}^3$  region of the PDMS porous  
529 scaffold (always by employing the mosaic modality mentioned  
530 above) with the laser impinging this time the inner surface of  
531 the cross-cut, as depicted in the inset of Figure 5C. The two  
532 different views show the presence of omnidirectional cell  
533 clusters infiltrating both the superficial layers of the scaffold  
534 and the inner areas down to a depth  $\approx 2.2 \text{ mm}$  along the  $z$  axis  
535 and  $\approx 2 \text{ mm}$  along the  $y$  axis. A high-resolution video  
536 (“Video\_cross\_cut”) of the slices composing the 3D  
537 reconstruction is available in the Supporting Information.

#### 4. CONCLUSIONS

538 In this work, we reported a novel 3D structuration technique  
539 that provides a fast and cheap process to fabricate porous  
540 scaffolds made of a widely used biocompatible silicone such as  
541 PDMS. This technique involves a simple combination of water  
542 and silicone to form an emulsion that is further transformed  
543 into a highly porous scaffold using a two-step reticulation  
544 process. The fabrication takes place under temperature-/

pressure-controlled environment that could be easily scalable  
545 for mass production. Scanning electron microscopy character-  
546 ization provided a deep understanding of the different achieved  
547 morphologies confirming a control of the porous distribution  
548 associated with a hierarchical macro-micro structuration of the  
549 available surface that could have an impact on the biological  
550 perfusion and diffusion of nourishment. 3D morphological  
551 characterization was carried out by X-ray computed tomog-  
552 raphy and allowed to evaluate the general porosity and the size  
553 distribution of the pores as well as to investigate the  
554 interconnectivity of the PDMS porous scaffold. The format  
555 chosen to evaluate the performance of cell culture presented a  
556 general porosity of  $\sim 60\%$  with a  $\sim 98\%$  global interconnectiv-  
557 ity. Osteosarcoma SaOS-2 cells were seeded on the PDMS  
558 porous scaffold to evaluate the efficiency of the cell  
559 colonization and perfusion. SEM investigation in combination  
560 with fluorescence immune-staining imaging demonstrated a  
561 high level of cell adhesion and some features of advanced cell  
562 maturation. Two-photon confocal reconstruction displayed  
563 information about the cell colonization taking place within  
564 volumes of several  $\text{mm}^3$  in the inner core of the scaffold,  
565 proving a homogeneous tridimensional distribution of cells and  
566 their proliferation through all of the available pores.

As the fabrication process is simple, adapted with injection  
568 techniques, and amenable to large-scale production, we believe  
569 that it will open intriguing opportunities aiming at the  
570 integration of 3D porous scaffolds in bioreactors or micro-  
571 physiological systems. Further studies will be devoted to the  
572 impact of the scaffold porosity and architecture on inner flow  
573 patterns provided by microfluidic systems and subsequent  
574 studies on cell proliferation and differentiation.

#### 5 Supporting Information

3D model of the 3D-printed mold employed for the  
580 fabrication of the PDMS sample holder; SEM close-up  
581 images of the PDMS nest scaffold for different  
582 reticulation conditions; X-ray tomography analysis,  
583 porosity, and pore diameter distribution; and SEM and  
584 immunofluorescence characterization of SaOS-2 cells  
(PDF)

Video\_top\_surface (MP4)

Video\_cross\_cut (MP4)

Video\_liquid\_loading (MP4)

#### AUTHOR INFORMATION

##### Corresponding Authors

\*E-mail: [A.Accardo@tudelft.nl](mailto:A.Accardo@tudelft.nl). Phone: +31(0)152781610  
(A.A.).

\*E-mail: [laurent.malaquin@laas.fr](mailto:laurent.malaquin@laas.fr), [lmalaquin@laas.fr](mailto:lmalaquin@laas.fr). Phone: 594  
+33(0)561336384. Fax: +33(0)561553577 (L.M.). 595

##### ORCID

Thierry Leichle: 0000-0003-3183-8976

Angelo Accardo: 0000-0003-0442-3652

##### Present Address

<sup>1</sup>Department of Precision and Microsystems Engineering, 600  
Delft University of Technology, Mekelweg 2, 2628 CD Delft, 601  
The Netherlands (A.A.). 602

## 603 Author Contributions

604 The manuscript was written through contributions of all  
605 authors. All authors have given approval to the final version of  
606 the manuscript.

## 607 Funding

608 The present work was supported by the H2020 European  
609 project HOLIFab (Grant No. 760927). It was as well partly  
610 supported as part of the MultiFAB project funded by FEDER  
611 European Regional Funds and French Région Occitanie (grant  
612 agreement number: 16007407/MP0011594).

## 613 Notes

614 The authors declare no competing financial interest.

## 615 ■ ACKNOWLEDGMENTS

616 This work was partly supported by the LAAS-CNRS micro-  
617 and nanotechnologies platform member of the French  
618 RENATECH network. The authors acknowledge the support  
619 of Sophie Allart and Daniele Daviaud from the INSERM  
620 Centre de Physiopathologie de Toulouse-Purpan (CPTP) of  
621 Toulouse during the multiphoton confocal imaging acquisi-  
622 tions. They also acknowledge the support of FERMAT  
623 Federation to this work.

## 624 ■ REFERENCES

625 (1) Xiang, Z.; Cao, D. Porous Covalent–Organic Materials:  
626 Synthesis, Clean Energy Application and Design. *J. Mater. Chem. A*  
627 **2013**, *1*, 2691–2718.  
628 (2) Wang, W.; Zhou, M.; Yuan, D. Carbon Dioxide Capture in  
629 Amorphous Porous Organic Polymers. *J. Mater. Chem. A* **2017**, *5*,  
630 1334–1347.  
631 (3) Kim, S.; Lee, Y. M. Rigid and Microporous Polymers for Gas  
632 Separation Membranes. *Prog. Polym. Sci.* **2015**, *43*, 1–32.  
633 (4) Kaur, P.; Hupp, J. T.; Nguyen, S. T. Porous Organic Polymers in  
634 Catalysis: Opportunities and Challenges. *ACS Catal.* **2011**, *1*, 819–  
635 835.  
636 (5) Lande, B.; Mitzner, W. Analysis of Lung Parenchyma as a  
637 Parametric Porous Medium. *J. Appl. Physiol.* **2006**, *101*, 926–933.  
638 (6) Zhao, M.; Li, L. Dissecting the Bone Marrow HSC Niches. *Cell*  
639 *Res.* **2016**, *26*, 975–976.  
640 (7) Loh, Q. L.; Choong, C. Three-Dimensional Scaffolds for Tissue  
641 Engineering Applications: Role of Porosity and Pore Size. *Tissue Eng,*  
642 *Part B* **2013**, *19*, 485–502.  
643 (8) Zhu, D.; Handschuh-Wang, S.; Zhou, X. Recent Progress in  
644 Fabrication and Application of Polydimethylsiloxane Sponges. *J.*  
645 *Mater. Chem. A* **2017**, *5*, 16467–16497.  
646 (9) McDonald, J. C.; Anderson, D. C. D. J. R.; Chiu, D. T.; Wu, H.;  
647 Schueller, O. J. A.; Whitesides, G. M. Fabrication of Microfluidic  
648 Systems in Poly(Dimethylsiloxane). *Electrophoresis* **2000**, *21*, 27–40.  
649 (10) Jung, S.; Kim, J. H.; Kim, J.; Choi, S.; Lee, J.; Park, I.; Hyeon,  
650 T.; Kim, D.-H. Reverse-Micelle-Induced Porous Pressure-Sensitive  
651 Rubber for Wearable Human-Machine Interfaces. *Adv. Mater.* **2014**,  
652 *26*, 4825–4830.  
653 (11) Shi, J.; Zhang, H.; Jackson, J.; Shademani, A.; Chiao, M. A  
654 Robust and Refillable Magnetic Sponge Capsule for Remotely  
655 Triggered Drug Release. *J. Mater. Chem. B* **2016**, *4*, 7415–7422.  
656 (12) Liu, W.; Chen, Z.; Zhou, G.; Sun, Y.; Lee, H. R.; Liu, C.; Yao,  
657 H.; Bao, Z.; Cui, Y. 3D Porous Sponge-Inspired Electrode for  
658 Stretchable Lithium-Ion Batteries. *Adv. Mater.* **2016**, *28*, 3578–3583.  
659 (13) Liang, S.; Li, Y.; Chen, Y.; Yang, J.; Zhu, T.; Zhu, D.; He, C.;  
660 Liu, Y.; Handschuh-Wang, S.; Zhou, X. Liquid Metal Sponges for  
661 Mechanically Durable, All-Soft, Electrical Conductors. *J. Mater. Chem.*  
662 *C* **2017**, *5*, 1586–1590.  
663 (14) Duan, S.; Yang, K.; Wang, Z.; Chen, M.; Zhang, L.; Zhang, H.;  
664 Li, C. Fabrication of Highly Stretchable Conductors Based on 3D  
665 Printed Porous Poly(Dimethylsiloxane) and Conductive Carbon

Nanotubes/Graphene Network. *ACS Appl. Mater. Interfaces* **2016**, *8*,  
2187–2192.  
(15) Han, J.-W.; Kim, B.; Li, J.; Meyyappan, M. Flexible, 666  
Compressible, Hydrophobic, Floatable, and Conductive Carbon 668  
Nanotube-Polymer Sponge. *Appl. Phys. Lett.* **2013**, *102*, No. 051903. 670  
(16) McCall, W. R.; Kim, K.; Heath, C.; La Pierre, G.; Sirbully, D. J. 671  
Piezoelectric Nanoparticle–Polymer Composite Foams. *ACS Appl.* 672  
*Mater. Interfaces* **2014**, *6*, 19504–19509. 673  
(17) Bélanger, M. C.; Marois, Y. Hemocompatibility, Biocompati- 674  
bility, Inflammatory and in Vivo Studies of Primary Reference 675  
Materials Low-Density Polyethylene and Polydimethylsiloxane: A 676  
Review. *J. Biomed. Mater. Res.* **2001**, *58*, 467–477. 677  
(18) Mata, A.; Fleischman, A. J.; Roy, S. Characterization of 678  
Polydimethylsiloxane (PDMS) Properties for Biomedical Micro/ 679  
Nanosystems. *Biomed. Microdevices* **2005**, *7*, 281–293. 680  
(19) Vaysse, L.; Beduer, A.; Sol, J. C.; Vieu, C.; Loubinoux, I. 681  
Micropatterned Bioimplant with Guided Neuronal Cells to Promote 682  
Tissue Reconstruction and Improve Functional Recovery after 683  
Primary Motor Cortex Insult. *Biomaterials* **2015**, *58*, 46–53. 684  
(20) Zhou, J.; Ellis, A. V.; Voelcker, N. H. Recent Developments in 685  
PDMS Surface Modification for Microfluidic Devices. *Electrophoresis* 686  
**2010**, *31*, 2–16. 687  
(21) Halldorsson, S.; Lucumi, E.; Gómez-Sjöberg, R.; Fleming, R. M. 688  
T. Advantages and Challenges of Microfluidic Cell Culture in 689  
Polydimethylsiloxane Devices. *Biosens. Bioelectron.* **2015**, *63*, 218–  
690 231. 691  
(22) Lötters, J. C.; Olthuis, W.; Veltink, P. H.; Bergveld, P. The 692  
Mechanical Properties of the Rubber Elastic Polymer Polydimethylsi- 693  
loxane for Sensor Applications. *J. Micromech. Microeng.* **1997**, *7*, 145–  
694 147. 695  
(23) Merkel, T. C.; Bondar, V. I.; Nagai, K.; Freeman, B. D.; Pinnau, 696  
I. Gas Sorption, Diffusion, and Permeation in Poly(Dimethylsiloxane) 697  
The Permeability of Poly(Dimethylsiloxane) [PDMS] To. *J. Polym.* 698  
*Sci., Part B: Polym. Phys.* **2000**, *38*, 415–434. 699  
(24) Piruska, A.; Nikcevic, I.; Lee, S. H.; Ahn, C.; Heineman, W. R.; 700  
Limbach, P. A.; Seliskar, C. J. The Autofluorescence of Plastic 701  
Materials and Chips Measured under Laser Irradiation. *Lab Chip* 702  
**2005**, *5*, 1348. 703  
(25) Haycock, J. W. 3D Cell Culture: A Review of Current 704  
Approaches and Techniques. In *3D Cell Culture*; Humana Press, 705  
2010; pp 1–15. 706  
(26) McKee, C.; Chaudhry, G. R. Advances and Challenges in Stem 707  
Cell Culture. *Colloids Surf., B* **2017**, *159*, 62–77. 708  
(27) Ingber, D. E. Cellular Mechanotransduction: Putting All the 709  
Pieces Together Again. *FASEB J.* **2006**, *20*, 811–827. 710  
(28) Ranga, A.; Gobaa, S.; Okawa, Y.; Mosiewicz, K.; Negro, A.; 711  
Lutolf, M. P. 3D Niche Microarrays for Systems-Level Analyses of 712  
Cell Fate. *Nat. Commun.* **2014**, *5*, No. 4324. 713  
(29) Do, A.-V.; Khorsand, B.; Geary, S. M.; Salem, A. K. 3D Printing 714  
of Scaffolds for Tissue Regeneration Applications. *Adv. Healthcare* 715  
*Mater.* **2015**, *4*, 1742–1762. 716  
(30) Wang, Z.; Abdulla, R.; Parker, B.; Samanipour, R.; Ghosh, S.; 717  
Kim, K. A Simple and High-Resolution Stereolithography-Based 3D 718  
Bioprinting System Using Visible Light Crosslinkable Bioinks. 719  
*Biofabrication* **2015**, *7*, No. 045009. 720  
(31) Accardo, A.; Courson, R.; Riesco, R.; Raimbault, V.; Malaquin, 721  
L. Direct Laser Fabrication of Meso-Scale 2D and 3D Architectures 722  
with Micrometric Feature Resolution. *Addit. Manuf.* **2018**, *22*, 440–  
723 446. 724  
(32) Lemma, E. D.; Spagnolo, B.; De Vittorio, M.; Pisanello, F. 725  
Studying Cell Mechanobiology in 3D: The Two-Photon Lithography 726  
Approach. *Trends Biotechnol.* **2019**, *37*, 358–372. 727  
(33) Accardo, A.; Blatché, M. C.; Courson, R.; Loubinoux, I.; Vieu, 728  
C.; Malaquin, L. Two-Photon Lithography and Microscopy of 3D 729  
Hydrogel Scaffolds for Neuronal Cell Growth. *Biomed. Phys. Eng.* 730  
*Express* **2018**, *4*, No. 027009. 731  
(34) Accardo, A.; Blatché, M.-C.; Courson, R.; Loubinoux, I.; Vieu, 732  
C.; Malaquin, L. Direct Laser Fabrication of Free-Standing PEGDA- 733

- 734 Hydrogel Scaffolds for Neuronal Cell Growth: Engineering 3D  
735 Biocompatible Microenvironments. *Mater. Today* **2018**, *21*, 315–316.
- 736 (35) Accardo, A.; Blatché, M.-C.; Courson, R.; Loubinoux, I.;  
737 Thibault, C.; Malaquin, L.; Vieu, C. Multiphoton Direct Laser Writing  
738 and 3D Imaging of Polymeric Freestanding Architectures for Cell  
739 Colonization. *Small* **2017**, *13*, No. 1700621.
- 740 (36) Jia, W.; Gungor-Ozkerim, P. S.; Zhang, Y. S.; Yue, K.; Zhu, K.;  
741 Liu, W.; Pi, Q.; Byambaa, B.; Dokmeci, M. R.; Shin, S. R.; et al. Direct  
742 3D Bioprinting of Perfusible Vascular Constructs Using a Blend  
743 Bioink. *Biomaterials* **2016**, *106*, 58–68.
- 744 (37) Carve, M.; Wlodkowic, D. 3D-Printed Chips: Compatibility of  
745 Additive Manufacturing Photopolymeric Substrata with Biological  
746 Applications. *Micromachines* **2018**, *9*, 91.
- 747 (38) Tebboth, M.; Jiang, Q.; Kogelbauer, A.; Bismarck, A. Inflatable  
748 Elastomeric Macroporous Polymers Synthesized from Medium  
749 Internal Phase Emulsion Templates. *ACS Appl. Mater. Interfaces*  
750 **2015**, *7*, 19243–19250.
- 751 (39) Zargar, R.; Nourmohammadi, J.; Amoabediny, G. Preparation,  
752 Characterization, and Silanization of 3D Microporous PDMS  
753 Structure with Properly Sized Pores for Endothelial Cell Culture.  
754 *Biotechnol. Appl. Biochem.* **2016**, *63*, 190–199.
- 755 (40) Mohanty, S.; Larsen, L. B.; Trifol, J.; Szabo, P.; Burri, H. V. R.;  
756 Canali, C.; Dufva, M.; Emnéus, J.; Wolff, A. Fabrication of Scalable  
757 and Structured Tissue Engineering Scaffolds Using Water Dissolvable  
758 Sacrificial 3D Printed Moulds. *Mater. Sci. Eng., C* **2015**, *55*, 569–578.
- 759 (41) Dahlberg, T.; Stangner, T.; Zhang, H.; Wiklund, K.; Lundberg,  
760 P.; Edman, L.; Andersson, M. 3D Printed Water-Soluble Scaffolds for  
761 Rapid Production of PDMS Micro-Fluidic Flow Chambers. *Sci. Rep.*  
762 **2018**, *8*, No. 3372.
- 763 (42) Díaz Lantada, A.; Alarcón Iniesta, H.; Pareja Sánchez, B.;  
764 García-Ruiz, J. P. Free-Form Rapid Prototyped Porous PDMS  
765 Scaffolds Incorporating Growth Factors Promote Chondrogenesis.  
766 *Adv. Mater. Sci. Eng.* **2014**, *2014*, 1–10.
- 767 (43) Li, Q.; Duan, T.; Shao, J.; Yu, H. Fabrication Method for  
768 Structured Porous Polydimethylsiloxane (PDMS). *J. Mater. Sci.* **2018**,  
769 *53*, 11873–11882.
- 770 (44) Chen, I.-J.; Lindner, E. The Stability of Radio-Frequency  
771 Plasma-Treated Polydimethylsiloxane Surfaces. *Langmuir* **2007**, *23*,  
772 3118–3122.
- 773 (45) Kim, D. H.; Jung, M. C.; Cho, S.-H.; Kim, S. H.; Kim, H.-Y.;  
774 Lee, H. J.; Oh, K. H.; Moon, M.-W. UV-Responsive Nano-Sponge for  
775 Oil Absorption and Desorption. *Sci. Rep.* **2015**, *5*, No. 12908.
- 776 (46) Pedraza, E.; Brady, A.-C.; Fraker, C. A.; Stabler, C. L. Synthesis  
777 of Macroporous Poly(Dimethylsiloxane) Scaffolds for Tissue  
778 Engineering Applications. *J. Biomater. Sci., Polym. Ed.* **2013**, *24*,  
779 1041–1056.
- 780 (47) Pedraza, E.; Brady, A.-C.; Fraker, C. A.; Molano, R. D.; Sukert,  
781 S.; Berman, D. M.; Kenyon, N. S.; Pileggi, A.; Ricordi, C.; Stabler, C.  
782 L. Macroporous Three-Dimensional PDMS Scaffolds for Extrahepatic  
783 Islet Transplantation. *Cell Transplant.* **2013**, *22*, 1123–1135.
- 784 (48) Carnachan, R. J.; Bokhari, M.; Przyborski, S. A.; Cameron, N.  
785 R. Tailoring the Morphology of Emulsion-Templated Porous  
786 Polymers. *Soft Matter* **2006**, *2*, 608.
- 787 (49) Silverstein, M. S. PolyHIPEs: Recent Advances in Emulsion-  
788 Templated Porous Polymers. *Prog. Polym. Sci.* **2014**, *39*, 199–234.
- 789 (50) Rodan, S. B.; Imai, Y.; Thiede, M. A.; Wesolowski, G.;  
790 Thompson, D.; Bar-Shavit, Z.; Shull, S.; Mann, K.; Rodan, G. A.  
791 Characterization of a Human Osteosarcoma Cell Line (Saos-2) with  
792 Osteoblastic Properties. *Cancer Res.* **1987**, *47*, 4961–4966.
- 793 (51) Prideaux, M.; Wijenayaka, A. R.; Kumarasinghe, D. D.;  
794 Ormsby, R. T.; Evdokiou, A.; Findlay, D. M.; Atkins, G. J. SaOS2  
795 Osteosarcoma Cells as an in Vitro Model for Studying the Transition  
796 of Human Osteoblasts to Osteocytes. *Calcif. Tissue Int.* **2014**, *95*,  
797 183–193.
- 798 (52) Buades, A.; Coll, B.; Morel, J. M. In *A Non-Local Algorithm for*  
799 *Image Denoising*, Proceedings - 2005 IEEE Computer Society  
800 Conference on Computer Vision and Pattern Recognition, CVPR  
801 2005, 2005; Vol. II, pp 60–65.
- (53) Schlüter, S.; Sheppard, A.; Brown, K.; Wildenschild, D. Image  
802 Processing of Multiphase Images Obtained via X-Ray Micro-  
803 tomography: A Review. *Water Resour. Res.* **2014**, 3615–3639. 804
- (54) Varshney, N.; Sahi, A. K.; Vajanthri, K. Y.; Poddar, S.;  
805 Balavigneswaran, C. K.; Prabhakar, A.; Rao, V.; Mahto, S. K.  
806 Culturing Melanocytes and Fibroblasts within Three-Dimensional  
807 Macroporous PDMS Scaffolds: Towards Skin Dressing Material. *808*  
*Cytotechnology* **2019**, *71*, 287–303. 809
- (55) Wiggan, O.; Hamel, P. A. Pax3 Regulates Morphogenetic Cell  
810 Behavior in Vitro Coincident with Activation of a PCP/Non-  
811 Canonical Wnt-Signaling Cascade. *J. Cell Sci.* **2002**, *115*, 531–541. 812
- (56) Onesto, V.; Cancedda, L.; Coluccio, M. L.; Nanni, M.; Pesce,  
813 M.; Malara, N.; Cesarelli, M.; Di Fabrizio, E.; Amato, F.; Gentile, F.  
814 Nano-Topography Enhances Communication in Neural Cells Net-  
815 works. *Sci. Rep.* **2017**, *7*, No. 9841. 816
- (57) Onesto, V.; Villani, M.; Narducci, R.; Malara, N.; Imbrogno, A.;  
817 Allione, M.; Costa, N.; Coppè, N.; Zappettini, A.; Cannistraci, C.  
818 V.; et al. Cortical-like Mini-Columns of Neuronal Cells on Zinc Oxide  
819 Nanowire Surfaces. *Sci. Rep.* **2019**, *9*, No. 4021. 820
- (58) Kim, J.-H.; Seo, S.; Min, J. Epithelial Cell Patterns on a PDMS  
821 Polymer Surface Using a Micro Plasma Structure. *J. Biotechnol.* **2011**,  
822 *155*, 308–311. 823
- (59) Accardo, A.; Shalabaeva, V.; La Rocca, R. Colon Cancer Cells  
824 Adhesion on Polymeric Nanostructured Surfaces. *MRS Commun.* **825**  
**2018**, *8*, 35–39. 826
- (60) Schröder, H. C.; Boreiko, O.; Krasko, A.; Reiber, A.;  
827 Schwertner, H.; Müller, W. E. G. Mineralization of SaOS-2 Cells on  
828 Enzymatically (Silicatein) Modified Bioactive Osteoblast-Stimulating  
829 Surfaces. *J. Biomed. Mater. Res., Part B* **2005**, *75*, 387–392. 830
- (61) Barreau, C.; Labit, E.; Guissard, C.; Rouquette, J.; Boizeau, M.  
831 L.; Gani Koumassi, S.; Carrière, A.; Jeanson, Y.; Berger-Müller, S.;  
832 Dromard, C.; et al. Regionalization of Browning Revealed by Whole  
833 Subcutaneous Adipose Tissue Imaging. *Obesity* **2016**, *24*, 1081–1089. 834